# LASER PATH PLANNING AND POWER CONTROL STRATEGIES FOR POWDER BED FUSION SYSTEMS

H. Yeung[1], J. Neira[2], B. Lane[1], J. Fox[1], F. Lopez[1]

[1]Engineering Laboratory, [2]Physical Measurement Laboratory,
National Institute of Standards and Technology, Gaithersburg, MD 20899

## Abstract

In laser powder bed fusion additive manufacturing (AM) process, laser scan path, velocity, and power are some of the most important parameters affecting the build quality. Control strategies for laser path and power are implemented and tested on a prototype testbed based on industrial standard G-code type programming language (referred to as AM G-code). The proposed AM G-code demonstrates different modes which define power-velocity-position profiles, and account for the laser and scanner dynamics. AM G-code is interpreted into *xy2-100* protocol and sent to the galvo scanners and laser using a custom transmitter. The actual scan path is compared with the commanded path during controlled tests. The proposed AM G-code interpreter modes are then evaluated considering the measured dynamic system response, and further discussed in contrast to commercial powder bed fusion systems.

## Introduction

Laser powder bed fusion (LPBF) is an additive manufacturing (AM) process in which a focused, high power laser selectively melts geometric patterns into layers of metal powder, ultimately building a near fully dense freeform part. The LPBF fabrication process, and inherent resulting part quality, is determined by hundreds if not thousands of controlled and uncontrolled process parameters [1]. On a basic level, the laser control parameters (position, velocity, and power) and their respective synchronization, in conjunction with powder layer parameters (material, relative density, layer height, etc.) must be well-defined with certain combinations to adequately melt adjacent scan tracks and underlying substrate (or previously melted layers) to form fully dense solid parts. Many researchers have described various experimental approaches to determine appropriate parameter combinations, often termed 'process mapping' [2], which must be conducted for any new desired LPBF material.

Even when well-defined for near full density, varying the relative combination of these parameters can introduce known defects that plague LPBF parts. Pores, for example, have been attributed to various phenomena related to the power-velocity attributes or scan strategies (e.g., keyholing and collapse at high laser energy densities [3], or insufficient re-melting of adjacent scan vectors due to wide hatch spacing [4,5]. For example, Khairallah et al. noted that turning the laser off at the end of a scan vector can potentially cause pores to be trapped under the rapidly solidified melt pool, and recommended laser power decreased at these locations [6]. More adequately controlled velocity or power profiles along each scan vector can reduce probability of

---

pore formation, or provide a parametric space for other property optimization. Apart from solidification physics at the end of a single vector, the general size, shape, and timing of a laser scanning raster pattern are known to affect the melt pool thermal history of the part, thus the resulting local and global residual stress and microstructure [7–9]. Though commercial LPBF systems are rapidly improving and maturing, there is still wide potential fundamental research in melt pool, scan vector, and layer formation process physics.

To fully define scan strategies, a system must be able to control individual scan vectors, and to do that requires characterization of the galvo mirror and laser system dynamics, and subsequent synchronization. Commercial LPBF systems provide this calibration and synchronization; however, their controller software inherently imposes limits on scan strategy definition, since machines are primarily sold for part production rather than fundamental research. For this reason, the National Institute of Standards and Technology (NIST) is constructing an open architecture Additive Manufacturing Metrology Testbed (AMMT). The work described here describes the approach to achieve several objectives: 1) characterize the performance of the galvo scanner mirrors and laser for the AMMT, 2) develop initial building blocks for AMMT system control, including customized and fully defined scan vectors, and 3) demonstrate use of a potential standard open protocol for scan strategy definition.

## **Laser System**

### Galvo motors and mirrors

In LPBF AM process, a laser beam is directed by a pair of mirrors driven by galvo motors to achieve two-dimensional (x-y) scan, as shown in Figure 1. Galvo motors are limited rotation direct current (DC) torque motors optimized for high speed applications. The motors (mirrors) are rotated by the electromagnetic force proportional to the current flow in the motor coils. Closed-loop servo control is achieved through angular positon feedback from an internal encoder attached to the motor shaft. A proportional derivative (PD) control loop is usually implemented locally on the galvo driver board to quickly achieve target position without overshoot.
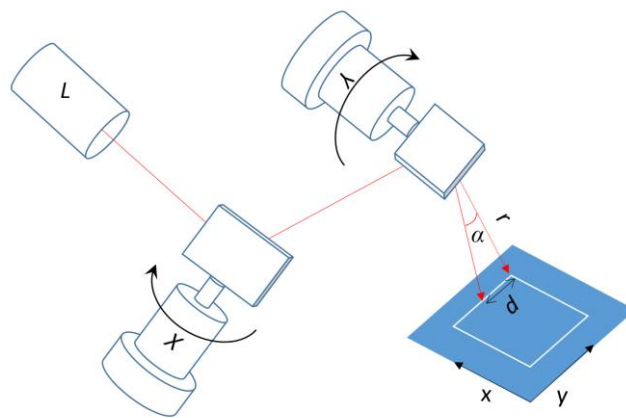


Figure 1: Typical scheme of a two-dimensional (x-y) optical scan system

## Scan control system

For a small angle mirror rotation (angle $\alpha$ in Figure 1), the surface scan distance d can be approximated by $d = r \cdot \alpha$, where $r$ is the traveling distance of the reflected laser beam and $\alpha$ is the rotation angle (Figure 1). If $r$ is large, $d$ is very sensitive to $\alpha$. In galvo control $\alpha$ is the command signal and usually represented by a +/- 5 V voltage. A digital protocol called *xy2-100* is often adapted to transmit this command voltage from the system controller (computer) to the galvo driver. The command voltages are packaged into 20-bit 'words' and transmitted at frequency ($f$) up to 100 kHz per 'word', or 2 Mbps; hence the galvo position is updated every $1/f$ second.
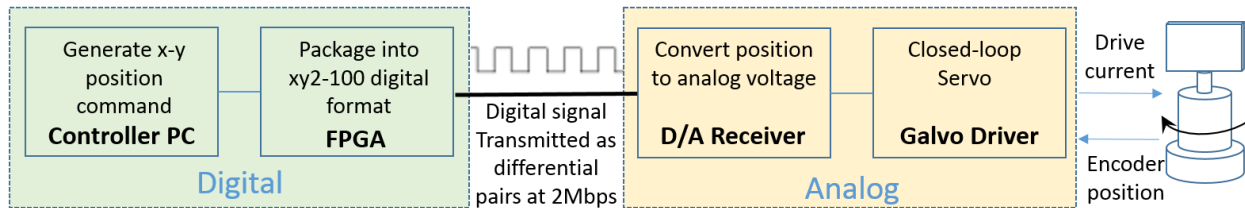


Figure 2: NIST AMMT laser control

Figure 2 shows the laser control implemented on the NIST AMMT. Scan lines/arcs are first converted into micro-steps (series of x-y positions) according to the predefined scan strategies on the Controller Personal Computer (PC). Each position is then packaged into *xy2-100* format on the Field Programmable Gate Array (FPGA) and transmitted through a differential signal transmitter. The digital positon signal is received by the Digital/Analog (D/A) Receiver and converted to analog voltage, and fed into the Galvo Driver as a command position to generate drive current to turn the mirror. The position detected by the galvo encoder is fed back to Galvo Driver to form a local closed servo loop. Most commercial LPBF AM systems have a similar design as Figure 2, except using proprietary software/hardware for path planning, x-y position generation, and *xy2-100* packaging.

To characterize the dynamic response of the galvo system, a high speed data acquisition system is set up to simultaneously capture the commanded position sent to the galvo driver (after D/A conversion) and the feedback (also referred to as measured) position from the galvo encoder (Figure 2).

## Velocity Profile

A similar rectangular path was scanned with both an off-the-shelf commercial scanner system and with the NIST AMMT prototyping system, respectively. On the commercial system, only galvo positions and speed can be set. On the NIST AMMT, galvo acceleration can also be defined. The scan results are shown in Figure 3, where the lines labeled $x_c, y_c$ and $x_m, y_m$ represent the command and feedback $x, y$ positions, respectively.
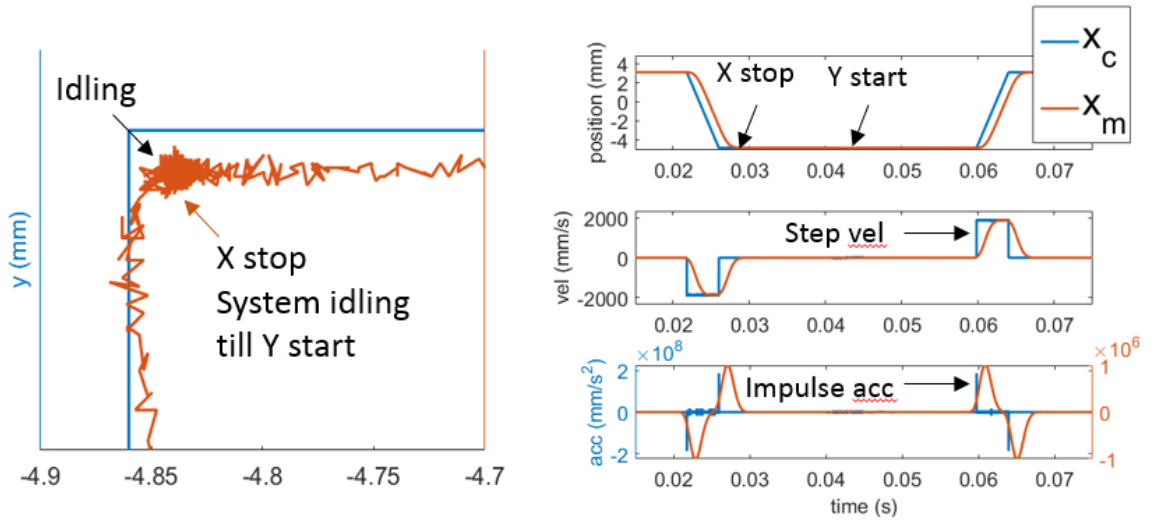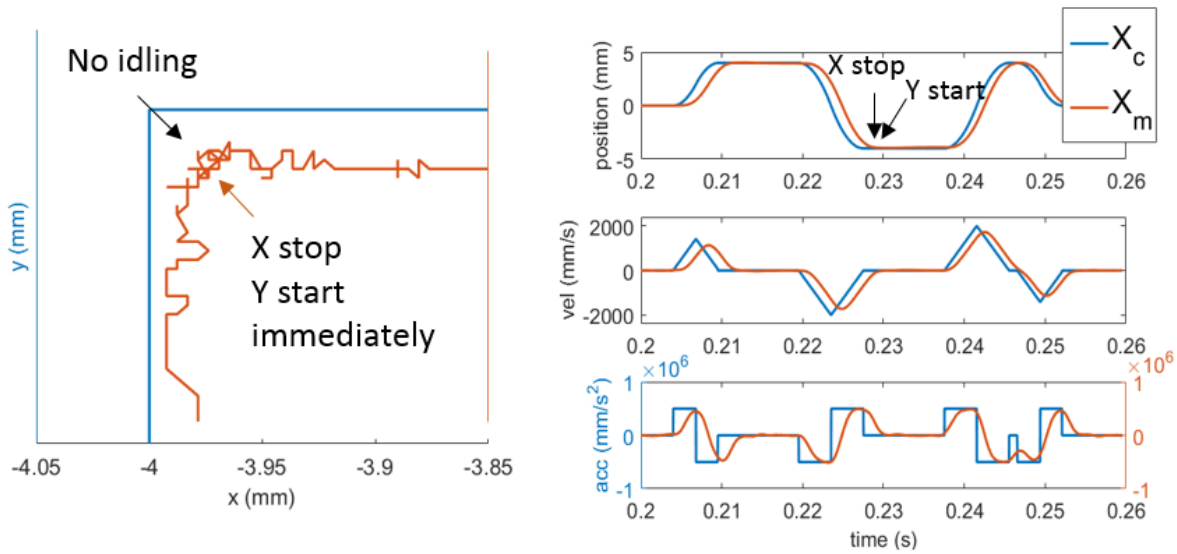
Figure 3: A rectangle scanned by (a) commercial scanner system, (b) NIST AMMT controller. Blue color represents the command position; orange is the encoder feedback position. Left side shows the x-y plot of upper left rectangle corner. Right side shows the *X* axis position, velocity, and acceleration profile.

Figure 3a reveals that for this particular commercial system, to make the corner scan on the left, infinite (impulse) acceleration was assumed and enough time was left for the galvo *X* to settle before the subsequent galvo *Y* move (marked as '*Y* start'). However, the lack of velocity profile monitoring such as on the NIST AMMT (Figure 3b), and unknown idling period, result in uncertainty in galvo position and velocity at a particular time, making the laser power-position synchronization difficult, and prevents implementation of more sophisticated control algorithms presented in the following.

<u>Frequency response</u>

A frequency varying (0 Hz to 600 Hz) sinewave of amplitude 1 mm was fed into galvo *X* and *Y,* respectively. The feedback amplitude and phase delay were analyzed by Fast Fourier Transform (FFT) and plotted against frequency in Figure 4a.

For a sinusoidal motion $X(t) = A\cdot\sin(2\pi\cdot f\cdot t)$, where *A* is the amplitude, *f* is the frequency, and t is the time, acceleration $a = -A\,(2\pi\cdot f)^2\sin(2\pi\cdot f\cdot t)$. Also, a phase delay (*dθ*) can be converted to time delay (*dt*) by $dt = d\theta/(2\pi\cdot f)$. Figure 4b plots the amplitude of commanded acceleration, amplitude of measured acceleration, and delay time for galvo *X* and *Y,* respectively.
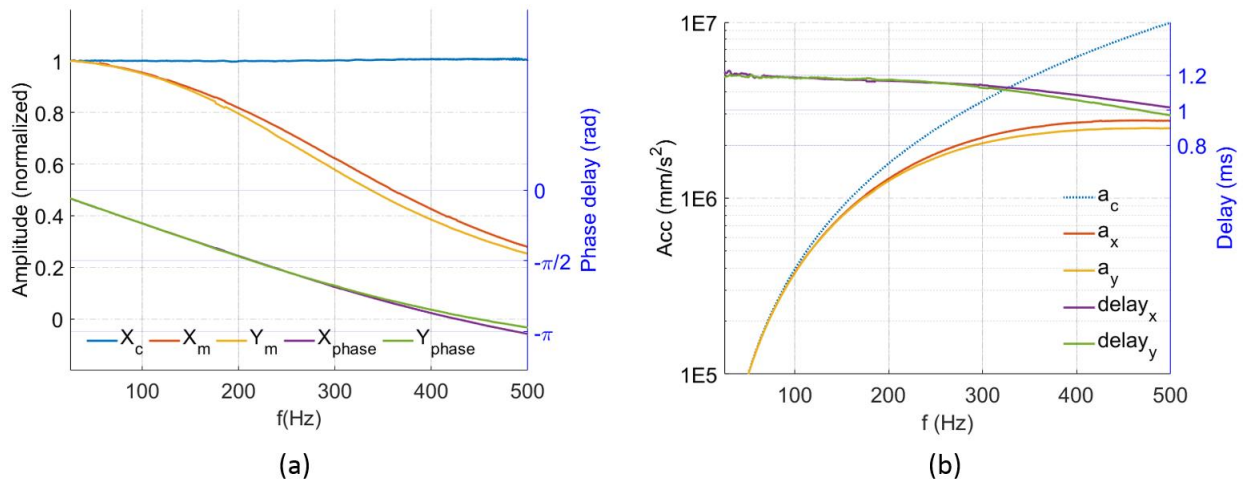


Figure 4: Frequency response analysis. (a) $x_c$ is the input amplitude, $x_m$ and $x_{phase}$ are feedback amplitude and phase delay for galvo *X*, $y_m$ and $y_{phase}$ are for *Y*. (b) $a_c$ is the input acceleration, $a_x$ and delay$_x$ are feedback acceleration and time delay for galvo *X*, $a_y$ and delay$_y$ are for *Y*.

Figure 4 shows galvo *Y* has a slightly slower response than galvo *X* at higher frequency. This could be caused by the larger mirror installed on galvo *Y*. At lower frequency ($< 100$ Hz), the response of Galvo *X* and *Y* are almost identical and follow closely (deviation $< 5\%$) to the command. The delay times are also relatively constant of 1.20 ms. These parameters were further verified with the laser power switched on, and position measured from the burning marks (discussed in the *Experimental* section).

The laser source is a 500 W 1070 nm Ytterbium fiber laser unit. Relative laser power is monitored with a silicon photo diode. It shows laser power can be varied at its full amplitude within 100 µs. This makes it possible to modulate laser power at each position step.

## **AM G-code**

Part of the rapid expansion and development of fused deposition modeling (FDM) plastic 3D printing is attributable to the RepRap and Maker communities [10]. Part of the utility of these systems, and contributor to the rapid adoption, is that they use a common control protocol so users of one system can quickly and rapidly program the toolpaths on different or new machines. G-code is the most commonly used numerical control (NC) programming language in motion control.

A G-code type programming language (referred to as AM G-code) is used to develop laser control on AMMT, with one additional keyword 'L' introduced to specify laser power. A detailed example of a G-code interpreter developed for 5-axis machining centers is given in [11]. Similar concepts, such as the G01 command for linearly interpolated motion, and G02/G03 command for clockwise / counter-clockwise circular interpolation, can be implemented for use in LPBF laser control, an example of which is shown in Figure 5. The arc window scan path in Figure 5a can be described by a 15 line AM G-code script in Figure 5b, compared to the 4476 line position commands of the *xy2-100* standard in Figure 5c.
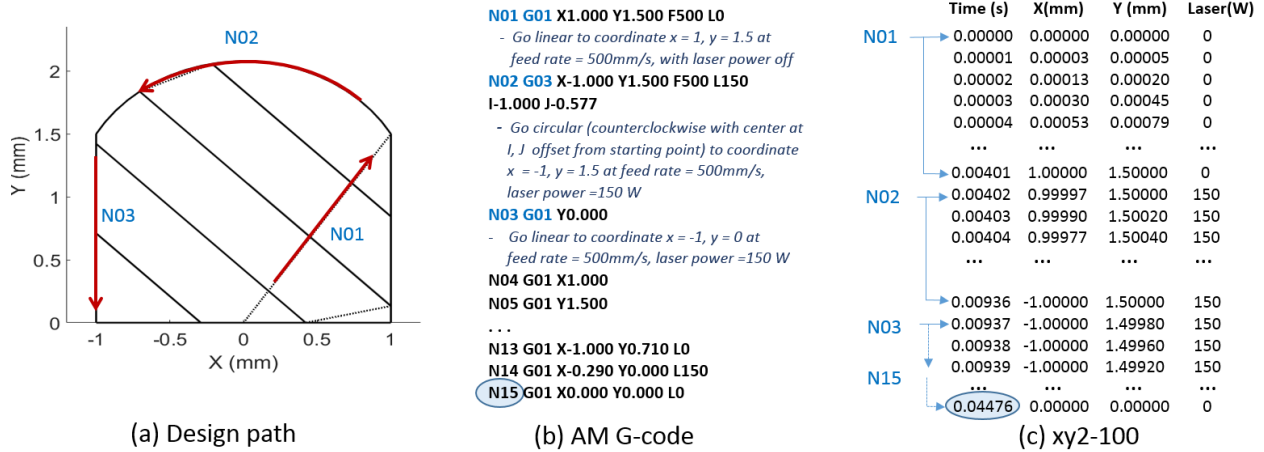


Figure 5: AM G-Code example. The scan path in (a) can described by the AM G-code in (b) and *xy2-100* commands in (c).

An AM G-code interpreter is developed to convert the AM G-code into position commands of *xy2-100* standard. G-code motion commands (e.g., G01, G02, and G03), are composed of a set of more basic commands (e.g., start, accelerate, hold velocity, decelerate, stop). In contrast to machining G-code motion commands, which mostly consist of velocity and position control, LPBF systems require definition of velocity/position and laser power control. For this reason, three laser path control modes and three laser power control modes are defined, implemented, and demonstrated.

Laser path modes

The following three laser path interpreter modes were devised, and example position/velocity plots modeled as demonstration:

1. Exact stop mode - control stops motion exactly at the end of each move with maximum allowable deceleration. If there is a subsequent move, the motion will start immediately again with maximum allowable acceleration until it reaches the programmed speed, or until it needs to decelerate again.

2. Continuous mode - control tries to match the ending velocity of the line or vector with the starting velocity of the subsequent line. In order to do so, move is allowed to deviate (overshoot) from the designed path within the maximum tolerance.

118

3. Constant build speed mode - control keeps the speed constant during the build move. Build move is defined as a move with laser power on. If the preceding move does not end with velocity that exactly matches the current build move, extra moves (with laser power off) with maximum allowable acceleration are introduced to match it.

Figure 6 below illustrate the three laser path modes. The same design path / AM G-code in Figure 5 can be interpreted into different scan moves based on the laser path mode selected.
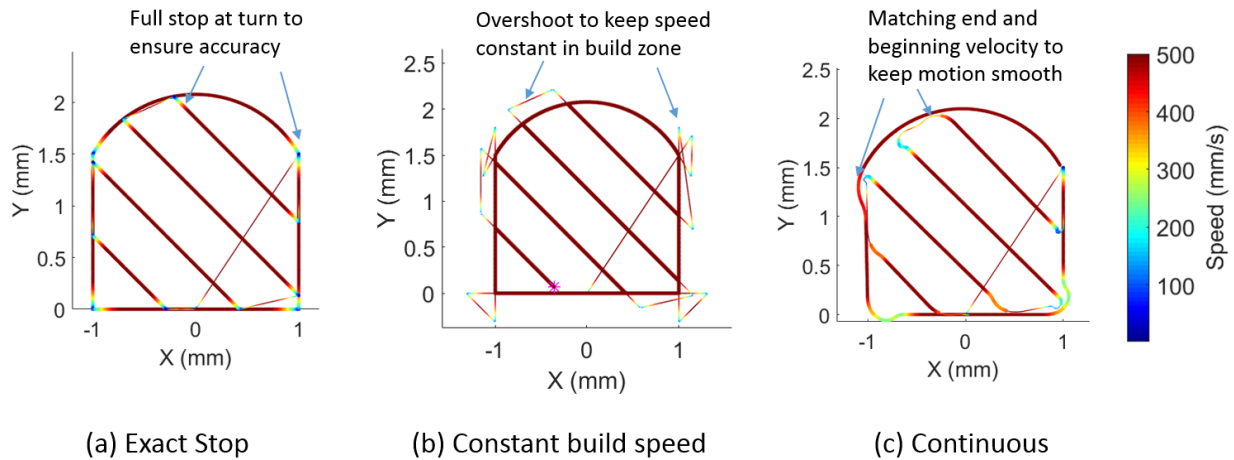


(a) Exact Stop        (b) Constant build speed        (c) Continuous

Figure 6: Laser path modes. (a) Exact stop. (b) Constant build speed. (c) Continuous. Speed variation is reprented by color

Laser power modes

Since laser power is an additional controllable parameter beyond position and velocity, new interpreter modes need to be devised. The following laser power interpreter modes were devised, with position/power plots modeled as demonstration.

1. Constant power mode - control keeps the power constant at the programmed level during each build move. If a subsequent move has a different power level, control sets the power to the new level.

2. Constant density mode - control keeps the power/speed ratio (power density) at a predefined constant during each move. This constant is not necessarily the same for all moves.

3. Thermal adjusted mode - control adjusts the power level according to the predefined thermal properties of the building process. For example, lower power at overhanging region, or raise power at initial stage while residual heat has not built up yet. It also provides a means for real time feedback control of power.

A simple thermal adjusted mode is implemented based on proximity. In Figure 7a, '$C$' marks the current laser position. Proximity of $C$ is evaluated based on distance $d$ between $C$ and each scanned point in the semi-sphere centered at $C$ and with predefined radius $r$. Sum of $(r - d)$ is used as a measurement for proximity. It is normalized and represented by color variation in

Figure 7a. If a metal plate is scanned, proximity can be used as an indicator of residual heat and laser power can be adjusted inversely proportional to it as shown in Figure 7b. More advanced thermal adjustment models can be developed in a similar way, and the time history factor of each scanned point can also be included.



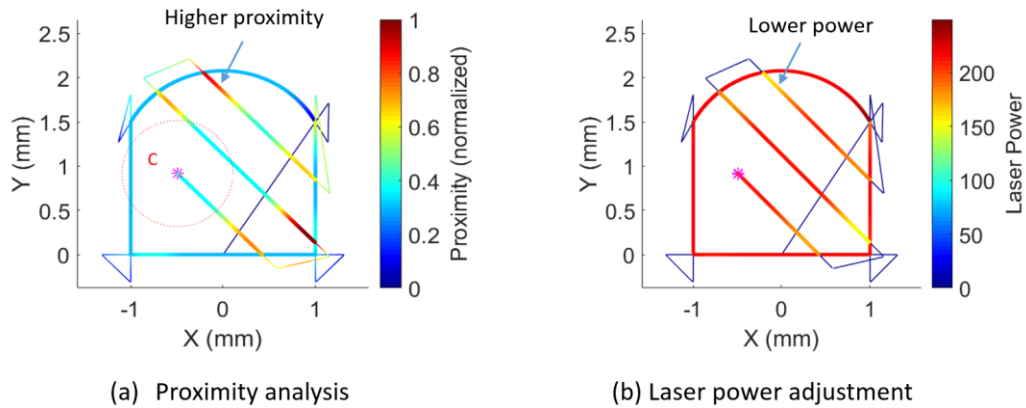(a) Proximity analysis    (b) Laser power adjustment

Figure 7: Demonstration of thermal adjusted laser power mode. (a) Proximity analysis based on distance of the evaluated point from its neighborhood. (b) Laser power adjustment based on proximity.

## Experiemental

Four sets of scan experiements were conducted on the NIST AMMT. The workpiece was a circular stainless steel plate of 115 mm diameter and 5 mm thickness, placed inside a sealed box purged with Argon (except the first experiment which was in air).

Galvo-Laser synchronization

This experiment was to demonstrate a way to synchronize laser power to the galvo position. Two trapezoids with hatch lines spaced at 1 mm were scanned on an unsynchronized system. The scan path and result are shown in Figure 8. Speed was set at 1000 mm/s and constant build speed mode was used, so time is linear proportional to distance within the borders of the trapezoid. The red arrows indicate where the laser was supposed to turn off if the system was synchronized. The laser was actually turned off 1.2 mm earlier (blue arrows). Therefore, the galvo-laser delay was found to be 1.20 ms. This agrees quite well with the delay time found by frequency response analysis (Figure 4b) in the *Frequency response* section. More accurate calibration can be achieved with more finely spaced hatch lines. A 1.20 ms laser power-on delay was introduced to synchronize laser power to position for later experiments.
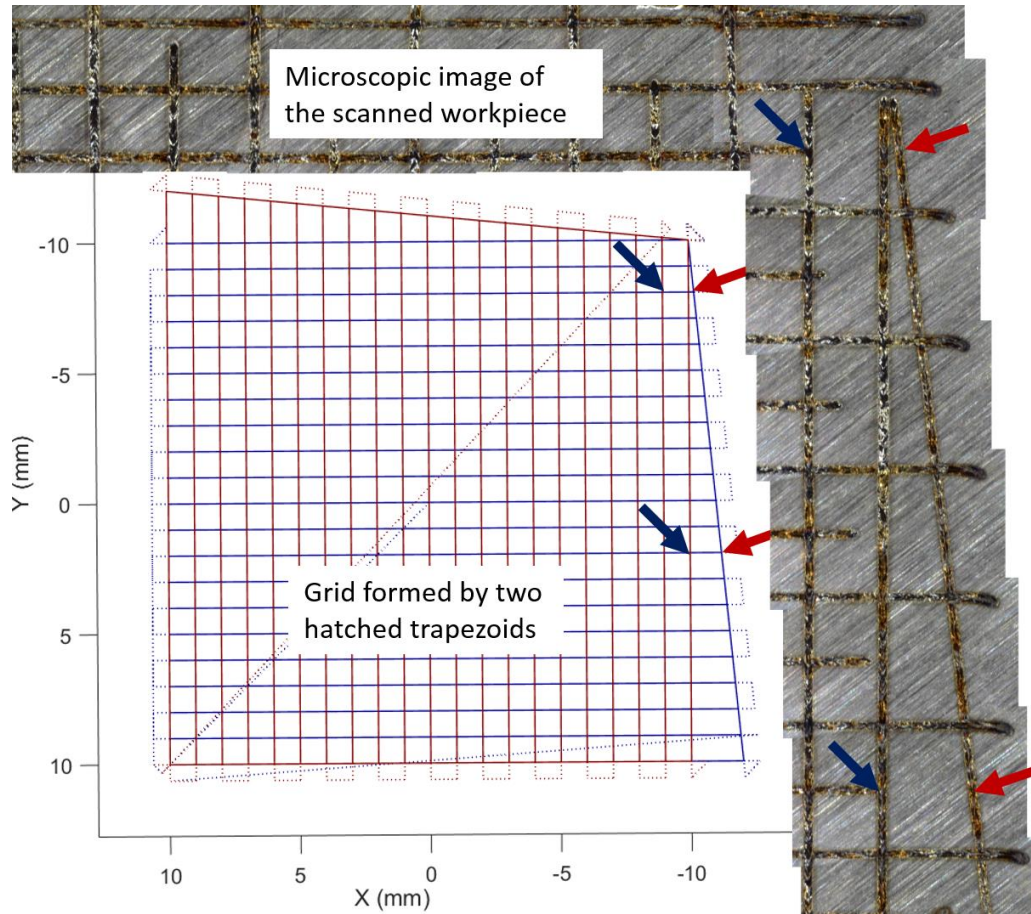
Figure 8: Calibration for galvo-laser delay. Two overlapped trapezoids with hatch lines (1 mm spacing) were scanned at 1000 mm/s. The red arrows indicate where the burnt lines were supposed to end, and blue arrows indicate where they actually ended. Therefore, laser power was turned off approximately1.20 mm (or 1.20 ms) earlier.

Power-speed process map

A power-speed process map is conducted to find out the feasible build range of AMMT, and also determine the effect of acceleration limitation on position accuracy. A crosshair pattern (Figure 10a) was scanned at 80 different speeds (200 mm/s to 2000 mm/s) and power (75 W to 250 W) combinations (Figure 9). The commanded line length and circle radius are 2 mm and 0.707 mm, respectively. The scans were done with constant build speed - constant power mode. Acceleration set for lines was $10^6$ mm/s$^2$. Acceleration was not constrained for circles. The scanned line length and circle radius were measured from images (Figure 9) and plotted against the commanded speed (Figure 10b). The commanded circle radius is noted as $r_c$, commanded line length as $l_c$, measured radius as $r_m$, and measured line length as $l_m$.
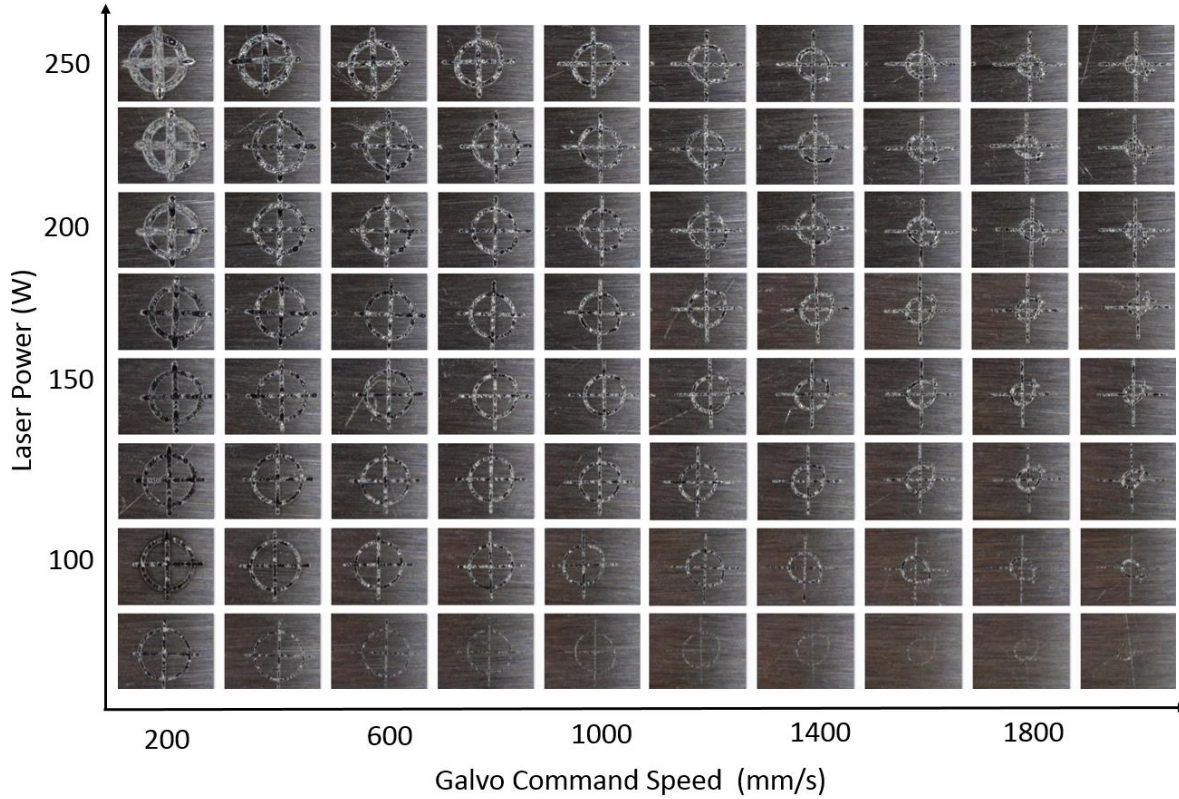
Figure 9: Power-speed process map. Power varies from 75 W to 250 W. Speed varies from 200 mm/s to 2000 mm/s. Same crosshair pattern was scanned at each power-speed setting.

As speed increases, $l_m$ stays closely to $l_c$ but $r_m$ drops rapidly from $r_c$. At 2000 mm/s, $l_m = 1.96$ mm, $r_m = 0.2$ mm (Figure 10b). A circular motion of radius $r$ and speed $v$ can be represented in x-y coordinates by $x(t) = r{\cdot}\cos(\omega{\cdot}t)$ and $y(t) = r{\cdot}\sin(\omega{\cdot}t)$, where $t$ is time, $\omega$ is angular velocity in rad/s and can be approximated by $v/r$. Acceleration $d^2x(t)/dt = -r{\cdot}\omega^2{\cdot}\cos(\omega{\cdot}t)$ and $d^2y(t)/dt = -r{\cdot}\omega^2{\cdot}\sin(\omega{\cdot}t)$. Therefore, to maintain a perfect circular motion, an acceleration with amplitude $a = r{\cdot}(v/r)^2$ is required for both $x$ and $y$ axis. As $v$ increases, eventually the galvo motor could not meet the required acceleration, the circular motion is distorted and a smaller $r_m$ results. $a_c = r_c\,(v/r_c)^2$ and $a_m = r_m{\cdot}(v/r_c)^2$ were defined as amplitude for commanded and measured acceleration and plotted in Figure 10b. Note, $r_m$ is not very accurately defined for a distorted circle, nor is $a_m$; but the maximum error should be within 42 %. During the AM G-code interpretation, arc speed can be constrained based on the $a_m$ value of the system to ensure accuracy.

It is interesting to compare the acceleration measurements from Figure 10b and Figure 4b. The points at which commanded acceleration $a_c = 5 \times 10^5$ were marked on both figures, and the corresponding measured acceleration was also noted (as 'actual'). For galvo $Y$ the acceleration found from frequency response (Figure 4b) is $4.76 \times 10^5$ mm/s$^2$, from the circle scan (Figure 10b) is $4.95 \times 10^5$ mm/s$^2$. Considering the possible radius measurement error (Figure 10a), it is very consistent and also demonstrates this process map can be a possible method for system calibration.
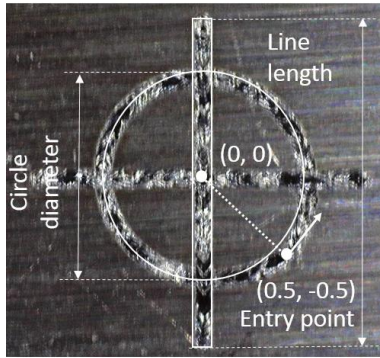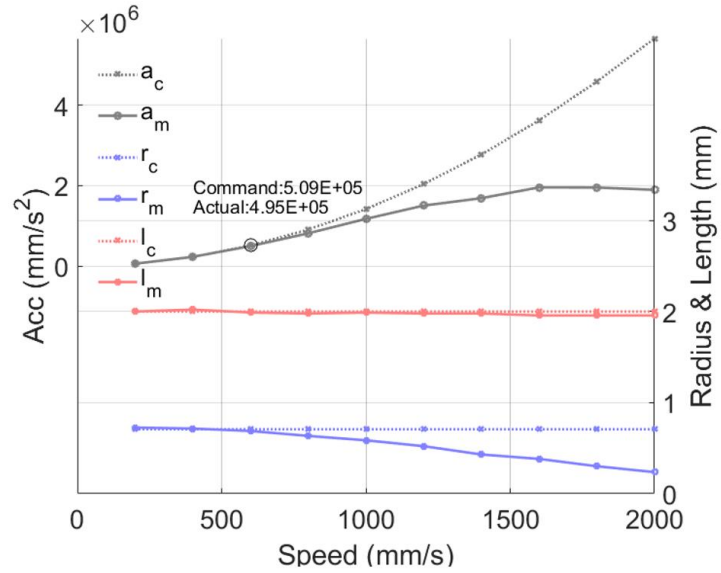
Figure 10: Effect of scanning speed on path accuracy. (a) Image shows a slightly distorted crosshair pattern scanned at power = 175 W and tangential speed = 800 mm/s. (b) $l_c$ and $l_m$ are the commanded and measured line length. $r_c$ and $r_m$ are the commanded and measured radius. $a_c$ and $a_m$ is the commanded and measured acceleration

AM modes

The arc window pattern in Figure 5 was scanned with the 3 x 3 combinations of scan path and laser power modes defined in the *AM G-code* section. Figure 11 shows the microscopic images for the bottom left corner of each scanned pattern. For each row the scan path is the same, only laser power varies; and vice versa for each column. The constant build speed path mode (first row) gives the most uniform bead, especially for the thermal adjusted power mode, since there is no swelling at the turn. However, a possible keyhole defect is observed at all three power modes (red arrows). This agrees with the prediction of [6], as in constant build speed mode the laser power is turned off immediately before the path overshoots. The gradually decreasing of laser power at the end of the scan is achieved in the exact stop path mode (third row). No keyhole is observed in any of these three power modes, but the corners are swollen (blue arrows), likely due to the excessive heat during slowing down. Further studies will be conducted to optimize the speed-power setting in exact stop - thermal adjusted mode to maintain the bead size as uniform as possible. It is not surprising to see the continuous path mode (middle row) actually gives the smoothest turn judged from the continuity of the bead (white arrows), although the price for this is accuracy, especially at higher velocity. Each mode has its pros and cons depending on the actual build requirements. The purpose here is to demonstrate the effect of different modes and the potential of incorporating them into a look-forward building strategy.
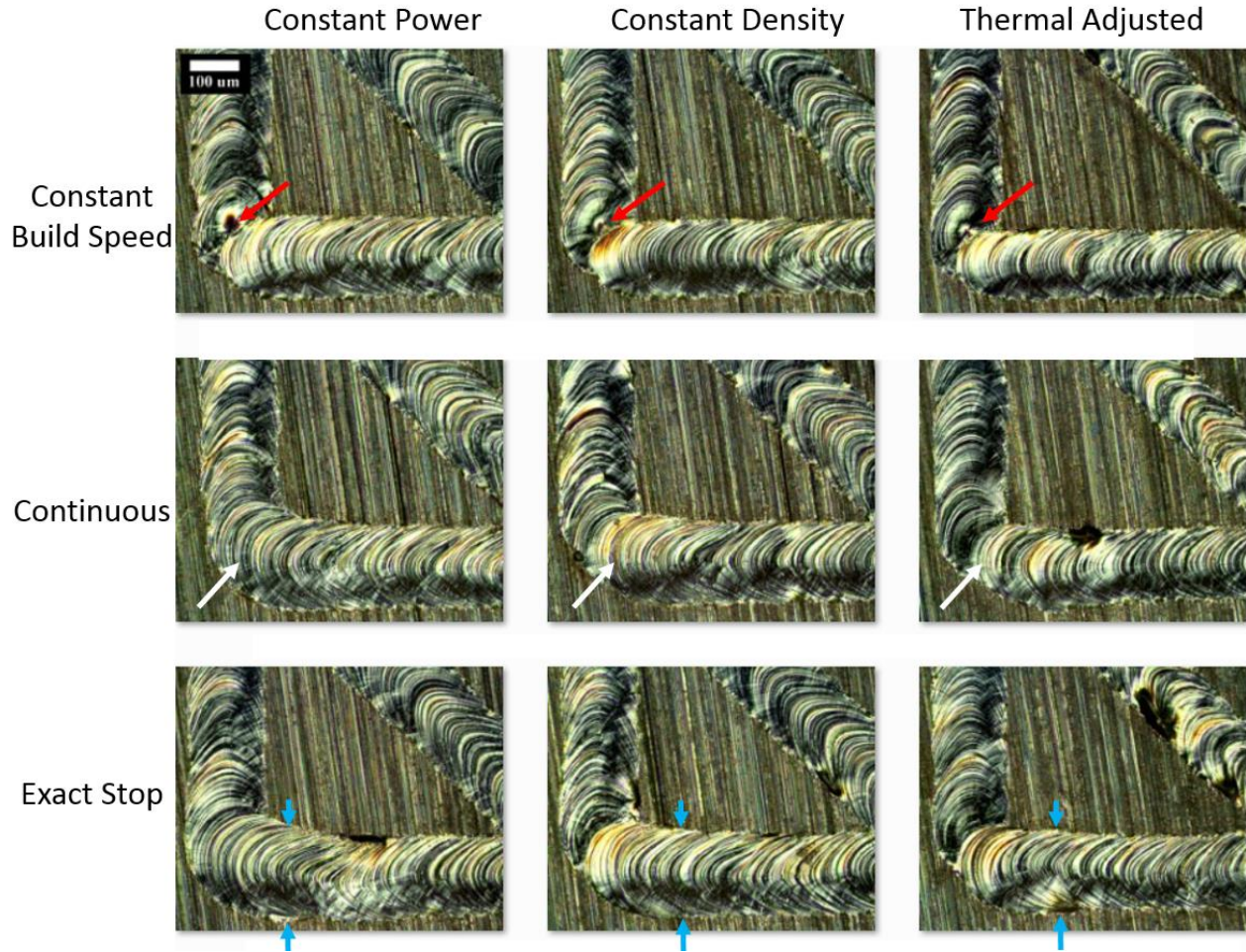
Figure 11: 3 x 3 combinations of scan path and laser power modes. The nominal scan speed is 500 mm/s, and maximum laser power is 250 W. The scale bar in the figure is 100 µm.

Scan with complicated strategies

Figure 12 shows a scan example on the AMMT with a combination of different modes. "NIST" was scanned with constant build speed - constant density mode, at 600 mm/s speed and 225 W maximum laser power. "AMMT/TEMPS" was scanned with continuous path - constant power mode, at 200 mm/s speed and 75 W laser power. G01, G02, and G03 were used to program linear and circular motions as illustrated in Figure 12b. 425 G-code lines were used to generate a 30 mm NIST logo and were interpreted into 218,507 *xy2-100* command lines. The G-code to *xy2-100* line ratio is approximately 1:500; and it will be 1:5000 if a 300 mm NIST logo is scanned. Comparing Figure 12b and Figure 12c, the bead size of "AMMT/TEMPS" was reduced to half simply through AM G-code parameter (speed/power) and interpretation mode settings. These are the programing efficiency and scan controllability that AM G-code can achieve.
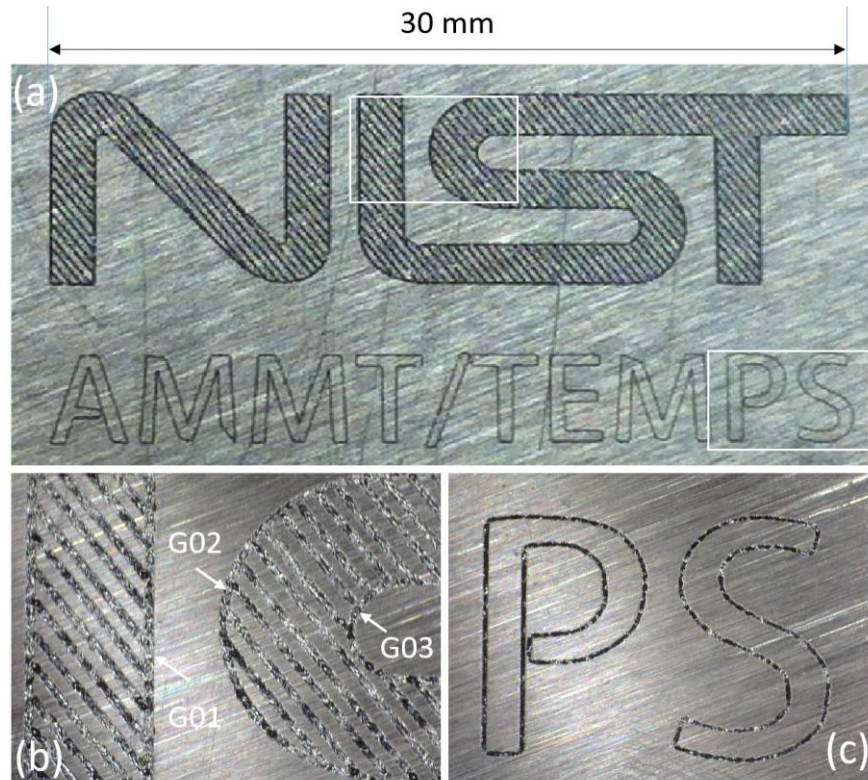
Figure 12: NIST logo was scanned at 600 mm/s, with constant build speed - constant density mode, at 225 W maximum laser power, with hatch size = 0.3 mm. AMMT/TEMPS was scanned at 200 mm/s, with continuous path - constant power mode, at 75 W laser power.

## Discussion and Summary

As mentioned in the *Introduction*, there is an open field of potential research into laser path planning, scan strategy, and laser power control, with potential to reduce the likelihood of defects, control residual stress or microstructure, or improve the speed and efficiency of material consolidation. To provide this capability, the NIST AMMT requires highly controlled and defined laser power position and speed. To realize this capability, this paper describes how the scanner mirror and laser system are characterized, and how laser path planning and power control strategies are implemented. The laser control system is based on the *xy2-100* protocol, where scanner position (path) and laser power are updated at each 10 µs interval (100 kHz). Rather than require position commands at 100 kHz, we chose to package commands into a standard protocol based on G-code, which is extensible to larger and more complex scan strategies. The AM G-code interpreter is defined with three path and three power interpretation modes to enable high level path / power programming without losing the controllability. The AMMT laser system was first characterized with varying frequency sinewave input and galvo encoder feedback; experiments were then conducted with scans programmed by AM G-code and measurements were made from microscopic images. The results are highly consistent, and also demonstrate the full controllability of power-velocity-position profiles through different modes. Although similar scan strategies may have been studied previously, building them into AM G-code interpretation modes can greatly

improve the efficiency and consistency of their implementation, provide controllability for the NIST AMMT, and provide an example for promotion and potential standardization of an open source machine command protocol.

Future research on the AMMT will also test and evaluate potential real-time feedback control methodologies, based on knowledge gained from fundamental scan strategy, and process monitoring research to determine optimal control strategies. With careful design, an *xy2-100* package (Figure 2) can be completed within 1 clock cycle, or 25 ns on a typical 40 MHz FPGA system. It can be done at real time immediately before each positon/power command update. This provides an opportunity to adjust these commands in real time before each update. The work presented here to deconstruct and re-build the laser and scanner control will not only provide controllability of the AMMT, but will support development of a platform to research real time feedback control strategies and algorithms, with an ultimate goal of being able to adjust laser power based on the melt pool feedback at the same rate as the power update (100 kHz).

## References

[1]   Mani M, Lane B, Donmez M A, Feng S, Moylan S and Fesperman R 2015 *Measurement science needs for real-time control of additive manufacturing powder bed fusion processes* (Gaithersburg, MD: National Institute of Standards and Technology)

[2]   Beuth J and Klingbeil N 2001 The role of process variables in laser-based direct metal solid freeform fabrication *JOM* **53** 36–9

[3]   King W E, Barth H D, Castillo V M, Gallegos G F, Gibbs J W, Hahn D E, Kamath C and Rubenchik A M 2014 Observation of keyhole-mode laser melting in laser powder-bed fusion additive manufacturing *J. Mater. Process. Technol.* **214** 2915–25

[4]   Thijs L, Verhaeghe F, Craeghs T, Humbeeck J V and Kruth J-P 2010 A study of the microstructural evolution during selective laser melting of Ti–6Al–4V *Acta Mater.* **58** 3303–12

[5]   Yadroitsev I, Thivillon L, Bertrand P and Smurov I 2007 Strategy of manufacturing components with designed internal structure by selective laser melting of metallic powder *Appl. Surf. Sci.* **254** 980–3

[6]   Khairallah S A, Anderson A T, Rubenchik A and King W E 2016 Laser powder-bed fusion additive manufacturing: Physics of complex melt flow and formation mechanisms of pores, spatter, and denudation zones *Acta Mater.* **108** 36–45

[7]   Cheng B, Shrestha S and Chou K 2016 Stress and deformation evaluations of scanning strategy effect in selective laser melting *Addit. Manuf.* In Press, Corrected Proof

[8]   Gockel J and Beuth J L 2013 Understanding Ti-6Al-4V microstructure control in additive manufacturing via process maps *Solid Freeform Fabrication Proceedings* Solid Freeform Fabrication Proceedings (Austin, TX) pp 666–74

[9]    Mercelis P and Kruth J-P 2006 Residual stresses in selective laser sintering and selective laser melting *Rapid Prototyp. J.* **12** 254–65

[10]  de Bruijn E 2010 On the viability of the Open Source Development model for the design of physical objects: Lessons learned from the RepRap project *Unpubl. DissMSc Thesis Tilburg Univ.*

[11]  Kramer T R, Proctor F M and Messina E 2000 *The NIST RS274/NGC Interpreter-Version 3*